AGU PUBLICATIONS

Water Resources Research

RESEARCH ARTICLE
10.1002/2016WR019279

Key Points:
- A coupled water-jet model is developed and validated with data from in situ oxygenation and mixing experiments in a stratified reservoir
- Mixing effects of the water-jet and bubble-plume systems on water thermal structure are investigated both experimentally and numerically
- A case study provides further insight into the mixing mechanisms of water-jet and bubble-plume systems

Supporting Information:
- Supporting Information S1

Correspondence to:
J. C. Little,
jcl@vt.edu

Citation:
Chen, S., C. Lei, C. C. Carey, P. A. Gantzer, and J. C. Little (2017), A coupled three-dimensional hydrodynamic model for predicting hypolimnetic oxygenation and epilimnetic mixing in a shallow eutrophic reservoir, *Water Resour. Res.*, *53*, 470–484, doi:10.1002/2016WR019279.

Received 31 MAY 2016
Accepted 17 DEC 2016
Accepted article online 26 DEC 2016
Published online 18 JAN 2017

A coupled three-dimensional hydrodynamic model for predicting hypolimnetic oxygenation and epilimnetic mixing in a shallow eutrophic reservoir

Shengyang Chen[1], Chengwang Lei[1], Cayelan C. Carey[2], Paul A. Gantzer[3], and John C. Little[4]

[1]School of Civil Engineering, The University of Sydney, Sydney, New South Wales, Australia, [2]Department of Biological Sciences, Virginia Tech, Blacksburg, Virginia, USA, [3]Gantzer Water Resources Engineering, LLC, Kirkland, Washington, USA, [4]Department of Civil and Environmental Engineering, Virginia Tech, Blacksburg, Virginia, USA

Abstract Artificial mixing and hypolimnetic oxygenation are two common methods for improving water quality in reservoirs. To examine the effects of their operation on the thermal structure of the water column, we used a three-dimensional hydrodynamic model coupled with a newly developed water-jet model and an existing linear bubble-plume model in conjunction with whole-reservoir in situ mixing experiments in a drinking-water reservoir. This reservoir has a side-stream supersaturation (SSS) hypolimnetic oxygenation system and a bubble-plume epilimnetic mixing (EM) system installed to reduce hypolimnetic hypoxia and algal blooms. The results show that the SSS successfully adds dissolved oxygen to the hypolimnion without destratifying the reservoir, whereas the EM, located at the lower metalimnetic boundary, deepens this boundary and partially mixes the metalimnion and epilimnion. The newly developed water-jet model coupled with the hydrodynamic model can successfully predict the variation of the thermal structure in the reservoir. The extent to which the SSS and EM systems affect the thermal structure of the reservoir is also quantified by further application of the coupled hydrodynamic model.

1. Introduction

Algal blooms and hypoxia impair the water quality of drinking water supply reservoirs [*Diaz*, 2001; *Vilhena et al*., 2010]. These water quality problems are closely interrelated: hypolimnetic hypoxia stimulates nutrient release from sediments, triggering algal blooms [*Gerling et al*., 2014; *Visser et al*., 2016]. After the blooms senesce, their decomposition further depletes dissolved oxygen (DO), thereby intensifying anoxic conditions [e.g., *Valiela et al*., 1997] and exacerbating nutrient release. In addition, DO depletion in the hypolimnion can cause the release of reduced iron and manganese from the sediments [*Davison*, 1993].

Various mixing and oxygenation systems are deployed in drinking water reservoirs to mitigate these water quality problems. Common oxygenation and mixing systems include bubble-plumes [*Singleton et al*., 2007], airlift aerators [*Burris et al*., 2002], Speece cones [*McGinnis and Little*, 1998], and side-stream oxygenation systems [*Fast et al*., 1975; *Gerling et al*., 2014]. Among these systems, the bubble-plume and side-stream supersaturation (SSS) hypolimnetic oxygenation systems have been shown to successfully improve water quality in lakes and reservoirs during stratified periods, with bubble-plume systems more successful in deeper water (with maximum depths greater than ~15 m) [*Singleton and Little*, 2006; *Singleton et al*., 2007] and SSS systems only recently shown to be successful in shallower water [*Gerling et al*., 2014]. However, the results have not always been satisfactory. Mixing induced by a side-stream pumping system, for example, caused premature destratification of the water column in some water bodies [*Lorenzen and Fast*, 1977; *Toffolon et al*., 2013]. Furthermore, Nürnberg et al. [2003] showed that improper mixing with devices operating continuously throughout the year increased phosphorus transfer from the hypolimnion to the epilimnion, thereby causing surface algal blooms.

Both mixing and oxygenation systems change the thermal structure of the water column, which alters the performance of the systems themselves, and can influence other biogeochemical processes, such as the sediment oxygen uptake rate [*Bryant et al*., 2011]. To account for these effects in design and operation, coupled hydrodynamic models are increasingly used [e.g., *Imteaz et al*., 2003; *Kerimoglu and Rinke*, 2013;

Singleton and Little, 2006]. However, many previous studies [e.g., *Hamilton and Schladow*, 1997; *Imteaz and Asaeda*, 2000; *Imteaz et al*., 2009] investigated artificial mixing in lakes or reservoirs using one-dimensional (1D) or two-dimensional (2D) numerical models, which may not fully resolve the non-homogeneous mixing in some water bodies. Using three-dimensional (3D) hydrodynamic models can more completely account for the effect of artificial mixing in reservoirs and lakes, achieving higher accuracy for model-predicted results compared to 1D or 2D models. Coupled bubble-plume/reservoir models are fairly well developed [e.g., *Singleton et al*., 2007, 2010], but those used for modeling SSS systems have not been as extensively studied [*Toffolon and Serafini*, 2013].

In this study, Si3D, a semi-implicit 3D hydrodynamic model originally developed for estuarine circulation, is employed to analyze a set of water quality management systems comprising a bubble-plume epilimnetic mixing (EM) system and a SSS hypolimnetic oxygenation system. A model for simulating the SSS system (water-jet model) is developed and coupled with Si3D, while a previously validated, coupled bubble-plume model [*Singleton et al*., 2007, 2010] is used to simulate the EM system in Si3D. In situ whole-reservoir experiments are carried out to validate the coupled water-jet model, to provide field data for understanding the mixing effects of both systems on thermal structure and DO, and to further validate the coupled hydrodynamic model with the bubble-plume and water-jet models operating in tandem in Si3D. Finally, the two coupled models are used to quantify the effect of mixing on the thermal structure in the reservoir, providing simple relationships that can be used in the design and operation of such water quality management systems. The present study is, to the best of our knowledge, the first to investigate an epilimnetic bubble-plume system using field experiments at a whole-reservoir scale, and is the first to examine the performance of both SSS and EM systems in one reservoir.

2. Field Experiments

2.1. Study Site and Oxygenation and Mixing Systems

Falling Creek Reservoir (FCR) is a eutrophic, shallow, drinking-water reservoir (maximum depth of 9.3 m and mean depth of 4 m) managed by the Western Virginia Water Authority in Vinton, Virginia, USA (37°18′20″N, 79°50′19″W). During the stratified period, FCR experiences persistent hypolimnetic hypoxia and occasional algal blooms [*Gerling et al*., 2014, 2016]. An increase in algae leads to shorter filter run times as well as taste and odor problems, while hypoxia leads to increased levels of soluble iron, manganese, and phosphorus in the hypolimnion [*Matthews and Effler*, 2006; *McGinnis and Little*, 2002; *Mortimer*, 1941].

FCR is equipped with SSS and EM systems to mitigate these water quality problems (Figure 1). Figure 1 also shows the typical thermal structure in the reservoir, which includes the epilimnion and hypolimnion, and the metalimnion between the two layers. For brevity, we define the *metalimnetic boundary* as the lower boundary of the metalimnion (close to the seasonal thermocline as shown in *Monismith et al*. [1990]), which is determined following the method described by Read et al. [2011]. The SSS system is designed to add DO to the hypolimnion and suppress the release of soluble iron, manganese, and phosphorus from the sediments, with minimal interference on thermal structure in the water column. The purpose of the EM system is to simultaneously mix and deepen the surface mixed layer above the metalimnetic boundary, and to redistribute algal species vertically, thereby limiting light and nutrient availability for the growth of algae [*Visser et al*., 2016]. It is believed that an unstable environment (i.e., vertical mixing) created by the EM system hinders the growth of bloom-forming cyanobacteria in stratified water bodies [*Walsby*, 2005; *Walsby et al*., 2006] though some phytoplankton taxa (e.g., diatoms) may be favored by decreased stability of the water column [*Imteaz et al*., 2009]. Air is used in the EM system to generate the bubble plume.

The SSS system consists of six main components: a submersible pump, inlet piping, oxygen source, oxygen contact chamber, outlet piping, and distribution header with nozzles oriented at an angle of 10° above horizontal to minimize turbulence near the sediments. The full SSS description is provided elsewhere [*Gerling et al*., 2014]. The EM system consists of two main components: a compressed air system located on land and a distribution header located in the reservoir, as described in the supporting information, Text S1. The SSS distribution header was located in the hypolimnion ∼1 m above the sediments, while the EM diffuser was positioned at ∼5 m below the water surface, which at the time of operation was at the depth of the metalimnetic boundary.

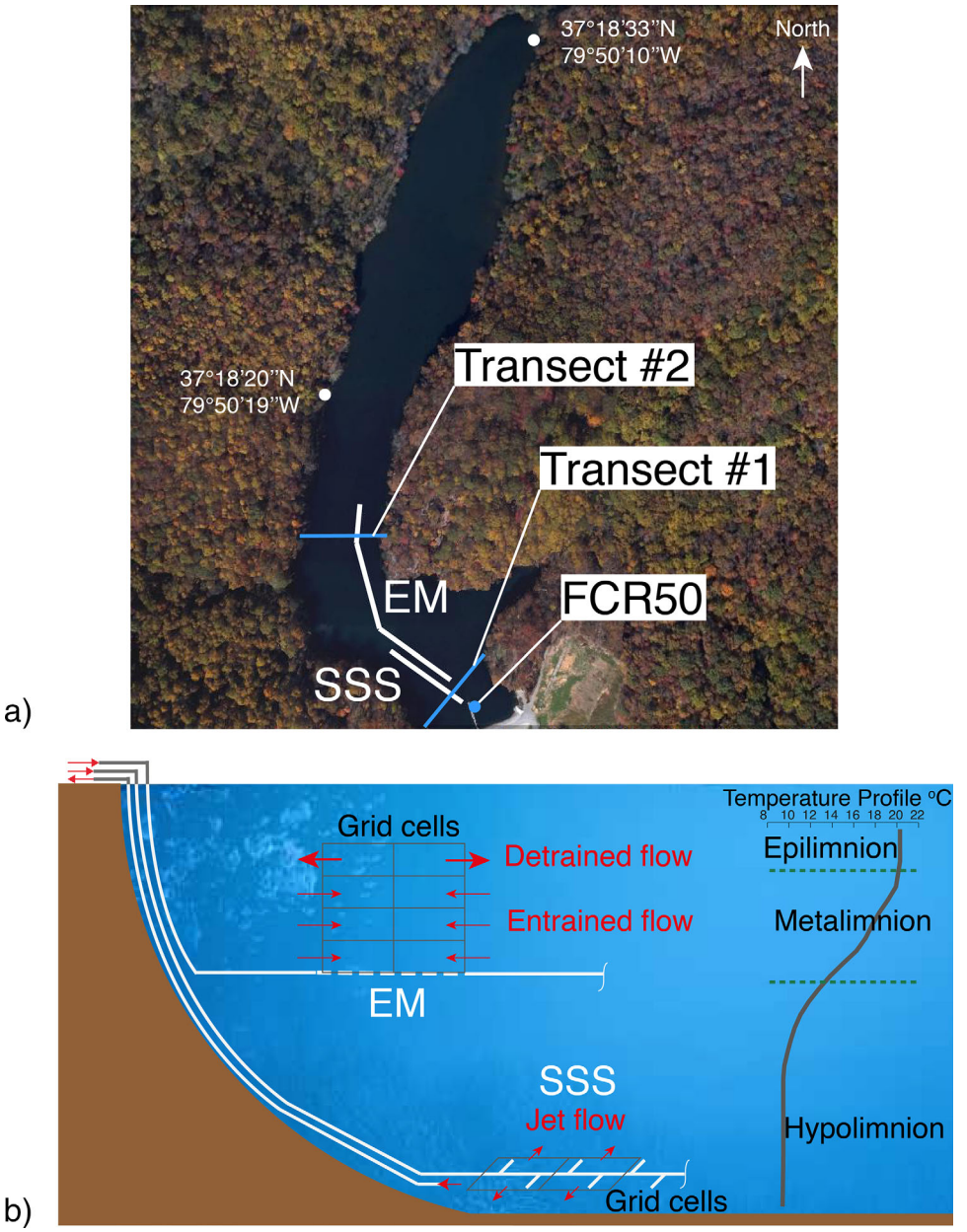

Figure 1. (a) Locations of the SSS (short white line) and EM (long white line) systems in FCR as well as locations of two transects for data collection. The sampling point FCR50 is the deepest point in the reservoir near the intake for the water treatment plant. (b) Schematic diagram showing the locations of the SSS distribution header and the EM diffuser in water column. The white lines show where the diffusers are deployed, whereas the solid rectangles indicate grid cells in the coupled hydrodynamic model. The flows induced by the systems are indicated by red arrows. The green dotted line between the metalimnion and hypolimnion in the temperature plot indicates the lower metalimnetic boundary.

2.2. Field Data Collection

The field experiments were designed to effectively validate the coupled hydrodynamic models (described in Section 3) and to analyze the effects of mixing induced by the SSS and EM systems. Figure 1 shows the locations of the SSS distribution header and the EM diffuser in FCR as well as the locations of two transects where data were collected for quantifying the operational characteristics of the two systems. Monitoring locations shown in Figure 1a were in the deeper region of FCR. The sampling point FCR50 is the deepest point near the intake for the water treatment plant. The locations of Transects #1 and #2 across the diffuser lines were fixed in place with ropes running across the water surface.

Table 1. System Operation Schedule

DoY 2015	146–150	151	152	153	154
SSS @ 208 LPM	ON				
EM @ 708 LPM (25 scfm)		ON 3 h		ON 3h	

The field experiments were performed during the summer of 2015 (see Table 1), with the SSS and EM systems operated sequentially over a 9-day period, starting on 27 May 2015 (Day 146 of 2015) and ending on 4 June 2015 (Day 154 of 2015). During this period, the SSS system produced a water flow rate of 208 liters per minute (LPM) for about 6 days. It was then turned off at noon on Day 151. The EM system was immediately turned on for a first period of 3 h at an air flow rate of about 708 LPM (equivalent to 25 standard cubic feet per minute). The EM system was then turned off for 2 days, and finally turned back on again at the same flow rate for a second 3-h period. While the SSS system was running continuously during the 6-day period, the EM system was only operated intermittently for the two short periods because the EM system had not been extensively tested in the field and there was concern about potential premature destratification, which would disrupt the operation of the drinking-water treatment plant.

The field data collected included water temperature, DO, and meteorological data. Field measurements were carried out using an SBE 19plus high-resolution (4 Hz sampling rate) Conductivity, Temperature, and Depth (CTD) profiler customized with a SBE 43 DO probe (Seabird Electronics, Bellevue, WA, USA) and a ProODO meter (YSI Inc., Yellow Springs, OH, USA). The CTD was used to collect depth profiles for temperature and DO. The response time of the CTD was 1.4 s at 20°C, enabling data to be collected at ~0.1 m increments in the water column. The ProODO meter was used to check the quality of the temperature and DO data collected using the CTD. The observational data were processed following the procedures described in [*Gerling et al*., 2014]. The meteorological data required for the numerical modelling were obtained from the weather station at Roanoke Airport, 11.8 km away from FCR, and were downloaded from the National Climatic Data Center, National Oceanic and Atmospheric Administration (NOAA, www.ncdc.noaa.gov/).

3. Numerical Model Formulation

The hydrodynamic model Si3D is based on Computational Fluid Dynamics and adopts an implicit finite-difference method for numerical solution of the Navier-Stokes equations. It has been comprehensively described [*Casulli and Cheng*, 1990; *Casulli and Cattani*, 1994; *Rueda et al*., 2007; *Smith*, 2006] and applied in many investigations of water flow in natural water bodies [e.g., *Rueda et al*., 2010; *Singleton et al*., 2010].

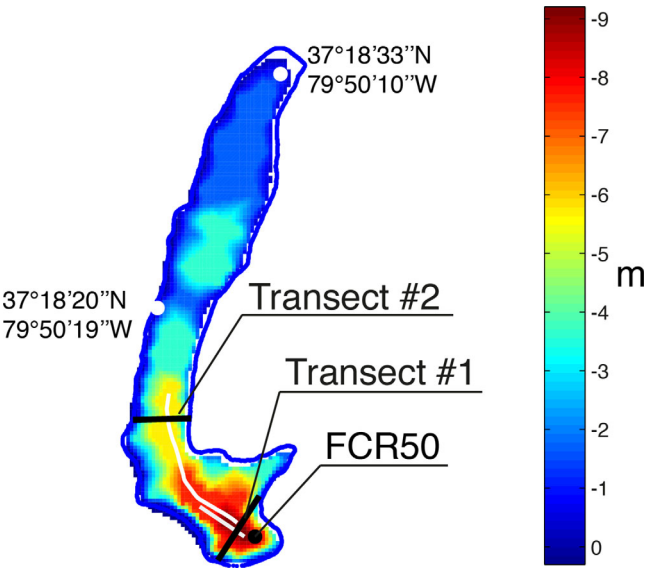

Figure 2. Numerical bathymetry and locations of the SSS system (short white line) and the EM system (long white line). The locations of FCR50 and Transects #1 and #2 from Figure 1 are also shown.

The numerical grid for Si3D was generated based on the FCR bathymetry, as shown in Figure 2. The grid cells are uniformly sized across the computational domain (4.5 m × 1.0 m × 0.3 m as shown in Figure 4). Si3D was verified in a numerical grid dependency test where three different grid resolutions were tested following the procedures described in Chen et al. [2014]. The current grid resolution was found to be sufficient and the numerical error for the quantities of interest is negligible. The monitoring locations in the model are the same as those in the field measurements, as shown in Figure 2. As mentioned earlier, coupled models are used to simulate the operation of the SSS and EM systems in FCR. The new water-jet model for the SSS system is based on jet-flow theory, and will be described in detail, whereas the

bubble-plume model for the EM system will only be briefly reviewed, as it has already been described in detail in the literature [e.g., *Singleton et al*., 2007; *Wüest et al*., 1992].

3.1. Coupled Water-Jet Model for SSS and Its Validation

The coupled water-jet model is designed to resolve the small-scale jet flow with the much larger grid cells in the hydrodynamic model. Each grid cell is about 150 and 30 times the diameter of the jet nozzle (b_0) in the longitudinal and transverse directions, respectively.

During operation of the SSS system, water is withdrawn by a submersible pump in the hypolimnion and passed through a pipe to an oxygen contact chamber on the shore where oxygen is added to the water [*Gerling et al*., 2014]. A grid cell at the pump location serves as a sink for water to simulate the water withdrawal by the submersible pump. The oxygenated water is returned to the hypolimnion through nozzles on both sides of the distribution header, forming a linear diffuser. Jets are formed in the stratified water body emanating from each of the nozzles along the distribution header. The jet flow entrains ambient water and expands as it penetrates the surrounding water (Figure 3). The jet nozzle is assumed to be at the center of a jet cell consisting of three grid cells which collectively serve as a point source in the hydrodynamic model (Figure 4).

The water-jet model is developed based on jet-flow theory [*Morton et al*., 1956; *Paillat and Kaminski*, 2014]. As shown in Figure 3, the coupled water-jet model accounts for ambient flow induced by the nozzle and discharge of oxygen-rich water from the nozzle. In addition to the momentum induced by the jet discharge, the model also resolves the ambient flow entrained by the expanding jet.

The general mass and momentum conservation equations for any point source are [*Morton et al*., 1956]:

$$\frac{dQ_x}{dy} = q_e \tag{1}$$

$$\frac{dM}{dy} = \pi b^2 g(\rho_0 - \rho) \tag{2}$$

If the initial velocity profile from a round jet is uniform, the outflow is $Q_x = \pi b^2 v$ and the entrainment rate is $q_e = 2\pi b \alpha v$. Here α is the entrainment coefficient, the proportionality constant relating the inflow velocity at the edge of the jet flow to the horizontal velocity within the jet flow profile; v is the uniform velocity along the centerline of the jet nozzle within the effective radius b of the jet flow; and y is the centerline distance from the nozzle. Because the orientation angle of the nozzles is small and the density difference in the hypolimnion is minimal, it is assumed that $\rho \sim \rho_0$, and $dM/dy \sim 0$. Here M represents the momentum of the jet.

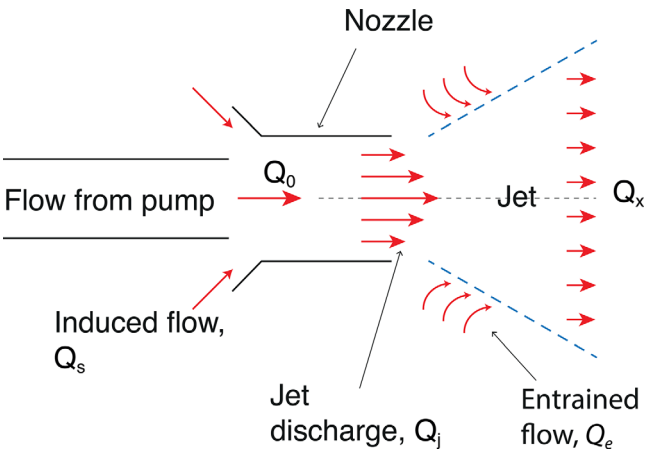

Figure 3. Sketch of the various flows associated with the water jets in FCR. The dashed horizontal black line indicates the center line of the jet. The flow rate out of the nozzle is $\boldsymbol{Q_j = Q_0 + Q_s}$. The total flow rate beyond the nozzle $(\boldsymbol{Q_x})$ consists of a flow rate out of the nozzle $(\boldsymbol{Q_j})$ and entrained flow $\boldsymbol{Q_e}$ from ambient water : $\boldsymbol{Q_x = Q_j + Q_e}$.

To predict the actual behavior of the jet flow from a round jet, a Gaussian function is used for the initial velocity profile [*Paillat and Kaminski*, 2014], which is subject to a normal distribution, or:

$$v(y,r) = v_m(y) e^{-r^2/b_e^2} \tag{3}$$

where $v_m(y)$ is the velocity at the jet axis when $r = 0$; e is Euler's number—an exponential growth constant; and b_e is a characteristic length of the jet profile measured from the axis of symmetry to points where the velocity amplitude is $1/e$ of that on the axis.

An effective radius (b_w) of the radial profile of the jet is defined, beyond which the velocity of the jet is

insignificant and can be neglected. To estimate the effective radius of the jet that is used to predict entrainment, it is assumed that $e^{-r^2/b_e^2} \sim 0$ when $r=b_w=3b_e$. The equation for the flow out of the nozzle can be expressed as:

$$Q_x(y)=\int 2\pi r v(y,r)dr=\int_0^{b_w} 2\pi r v_m(y)e^{-r^2/b_e^2}dr \tag{4}$$

Integrating equation (4) using the assumption above where $e^{-b_w{}^2/b_e^2}=0$ gives $Q_x(y)=\pi b_e^2 v_m(y)$, which can be rewritten as $Q_x=\pi b_e^2 v_m$. It is assumed that entrainment of water occurs at the characteristic length b_e of the jet, where the velocity is $\frac{1}{e}v_m$, so the entrainment rate is $q_e=2\pi b_e\alpha\left(\frac{1}{e}v_m\right)$. Therefore, equations (1) and (2) can be further developed and transformed to:

$$\frac{db_w^2 v_m}{dy}=\frac{6}{e}b_w\alpha v_m \tag{5}$$

$$\frac{db_w^2 v_m^2}{dy}=0 \tag{6}$$

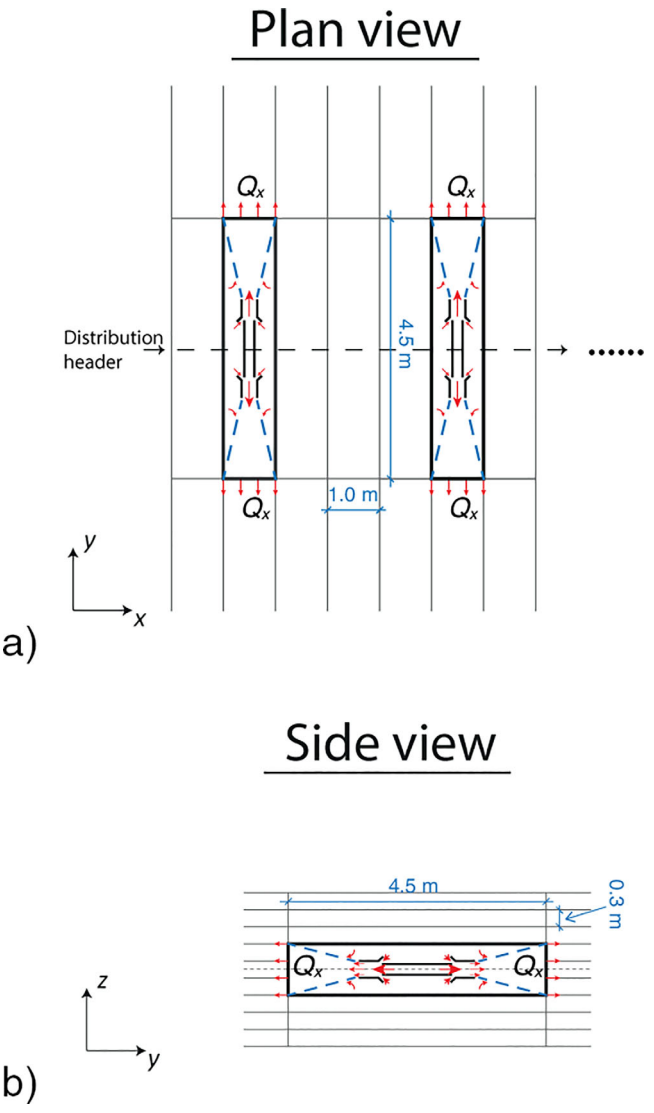

Figure 4. Schematic diagrams of the jet cells (bold rectangles) in the water-jet model with the grid cells shown behind (not to scale). The model resolves the flows described in Figure 3. (a) The dashed horizontal line indicates the distribution header of the SSS system. (b) The dashed horizontal line indicates the centerline of the jet.

A corresponding equation for the initial momentum of a jet (M_0) was also derived for the round jets using relationships presented in [*Xu and Antonia*, 2002]:

$$M_0=\int_0^{b_0}\rho v_0^2 2\pi r dr=\rho\pi b_0^2 v_0^2 \tag{7}$$

where v_0 is the jet velocity at the exit; ρ is the fluid density; and b_0 is the radius of the nozzle outlet.

By integrating the mass and momentum balance equations using the initial condition as shown in equation (7), the effective radius as a function of the centerline distance from the nozzle (y) and the centerline velocity (v_m) are calculated as:

$$b_w=b_0+\frac{6}{e}\alpha y \tag{8}$$

$$v_m=\frac{eb_0v_0}{eb_0+6\alpha y} \tag{9}$$

As shown in Figures 4a and 4b, a jet cell consists of two symmetrical jets. The size of the jet cell is determined by the approximate size of the jet (as indicated in Figure 3) when the stream-wise dimension of the jet profile becomes equivalent to the y dimension of the grid cells (Figure 4a). Afterward, the flow is resolved by the large-scale hydrodynamic model. First, the jet cell is matched to the jet profile. Based on equation (8), the radius of the expanding jet (b_w) is estimated from the travel

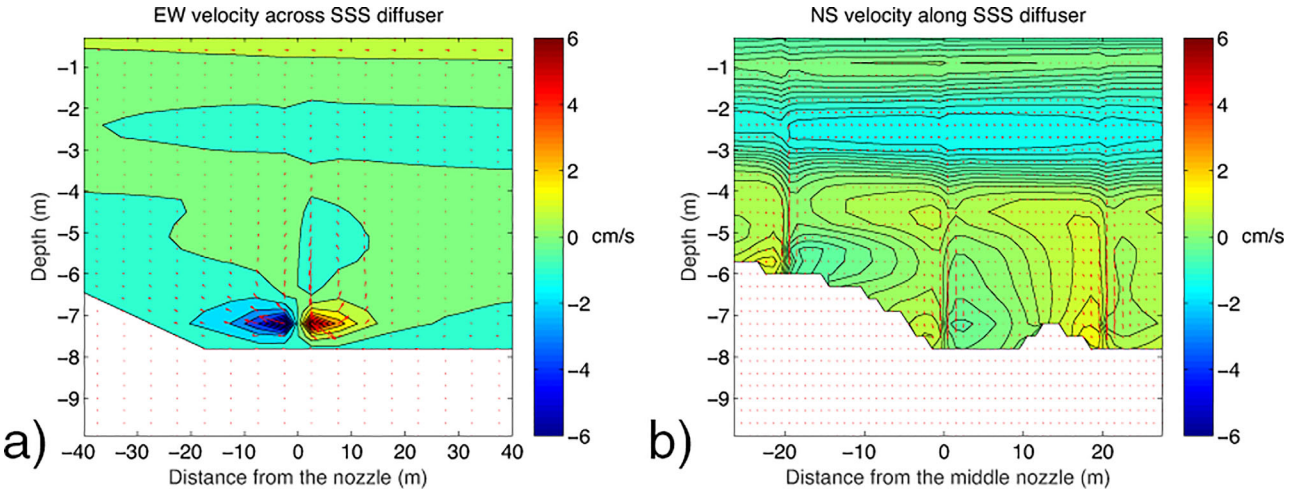

Figure 5. Numerical velocity field indicated by the contours of horizontal velocity magnitude and velocity vectors over (a) the section across the SSS distribution header and (b) the section along the SSS distribution header. The contour lines (black) in the figures indicate contour levels with an interval of 0.5 cm/s. The datum in the contours hereinafter is set at the water surface in a standard Cartesian coordinate system, hence the negative depths.

distance (y), which is half of the longitudinal length of the grid cell, and the expansion coefficient α, which is a constant with a value of 0.05 [*List*, 1982; *Wang and Wing-Keung Law*, 2002]. Since the jet is evenly expanding in both the horizontal and vertical directions, both the transverse (x) and vertical lengths (z) of the jet cell are the diameter of the radial profile of the expanding jet (b_w) calculated from equation (8). Second, the selected grid cells at the SSS location are combined to form jet cells. In the present model, the jet cell and grid cell are of the same size in the horizontal direction (Figure 4a). This means that the horizontal dimensions of the grid cells are the same as the jet cell so that the two symmetrical jet profiles are mapped into one grid cell in the plan view as shown in Figure 4a, which simulates the jet flow from both sides of the distribution header. To retain the vertical length scale of the jet cell, three consecutive grid cells in the vertical direction are combined to form one jet cell (Figure 4b). Finally after the jet cells are formed, the jet centerline velocity (v_m) is calculated using equation (9) associated with the radius of the nozzle (b_0) and the initial centerline velocity out of the nozzle (v_0), so that the flow out of the jet cell can be estimated.

The outflow Q_x from the jet cell to the adjacent grid cells is calculated from the centerline velocity at the exit face of the jet cell by a customized module in the Si3D code, which also converts the calculated Gaussian flow profile to an equivalent uniform profile, as required by the numerical model.

We validated the above-described coupled water-jet model by comparing the numerical velocity profiles to published results from physical experiments as well as some field data collected in FCR.

The contours of the numerically obtained horizontal velocity (Figure 5) show that the simulated jet flow behaves as expected, with ambient water entrainment by the jet consistently represented in the contours. The jet profiles in Figure 5 are consistent with the physically observed patterns of the radial profile of the jet in laboratory experiments [*Morton et al*., 1956; *Xu and Antonia*, 2002]. Moreover, the numerical data compare well to the field data (Figures 6 and 7) collected from FCR. Both the field and numerical contours in Figure 6 show that the SSS erodes the metalimnetic boundary, though the hypolimnetic temperature is not substantially increased. The field and numerical contours at Transect #1 (refer to Figures 7b and 7c) consistently show that the SSS lightly mixes the hypolimnion and starts to homogenize the hypolimnetic temperature across the deep region when compared to original profiles in Figure 7a. The variation between the field and numerical data within ± 5 m of the SSS line along Transect #1 was $\sim 0.02^{\circ}$C in terms of the mean temperature and $\sim 0.31^{\circ}$C in terms of the root-mean-square temperature. The difference between the field and numerical data in the mean temperature in the hypolimnion at FCR50 was less than 1% of the mean hypolimnetic temperature in the field when the SSS system was in operation.

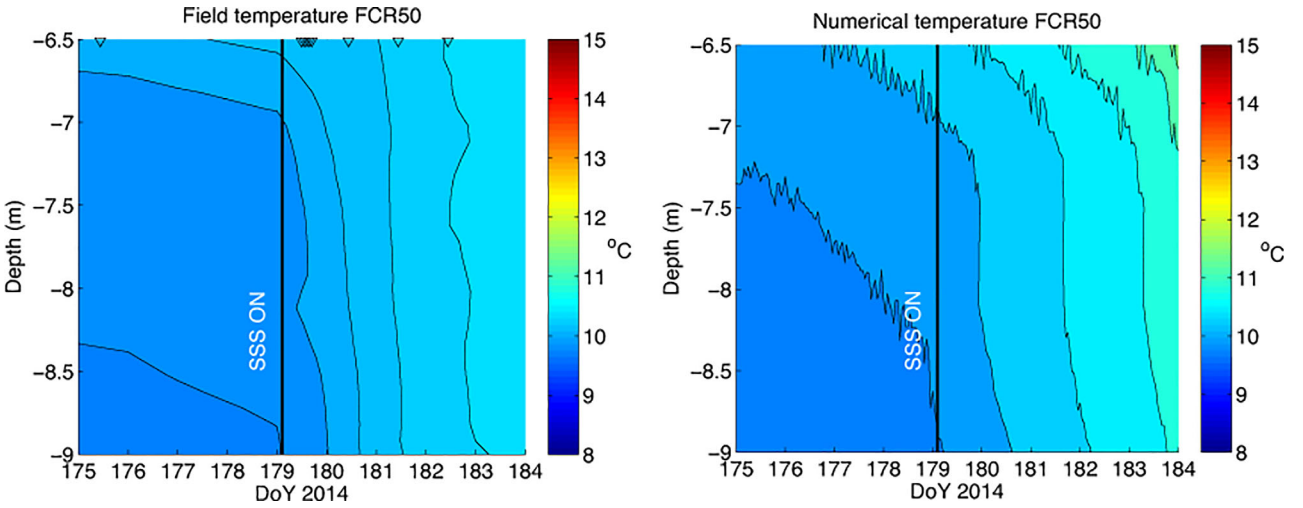

Figure 6. Time series of the field and numerical temperature contours at FCR50. The SSS was turned on from Day 179 of 2014 and ran continuously to Day 184 (contour level interval 0.5°C, the same interval for the rest of the temperature contours hereinafter).

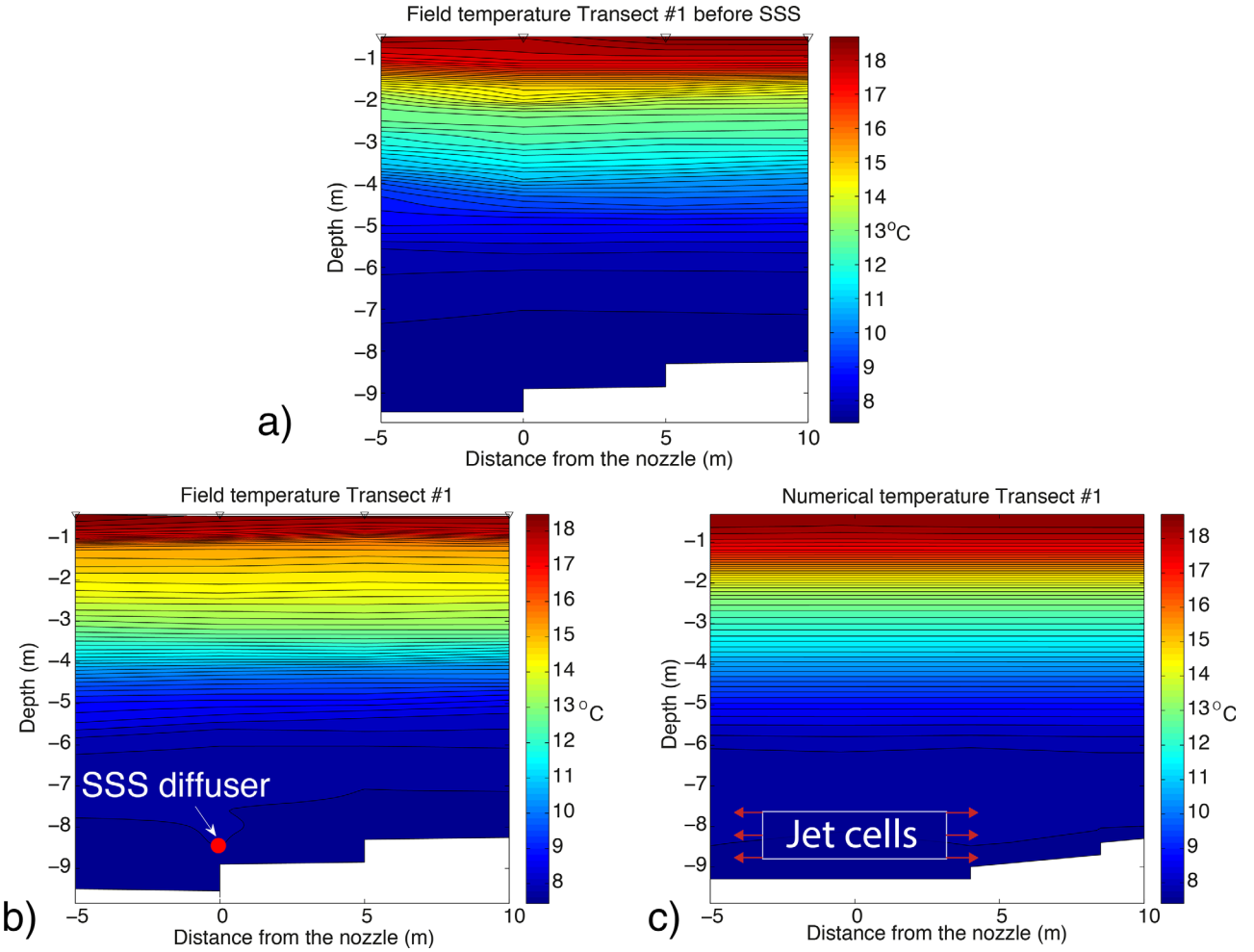

Figure 7. Temperature contours from Transect #1 at (a) before the SSS was turned on in 2015 (the numerical model was initialized based on this profiles); (b) 2 h after the SSS was turned on in the field; (c) 2 h after the SSS was turned on in the model. The sampling points are at −5, 0, 5, and 10 m from the distribution header in both the experimental and numerical results.

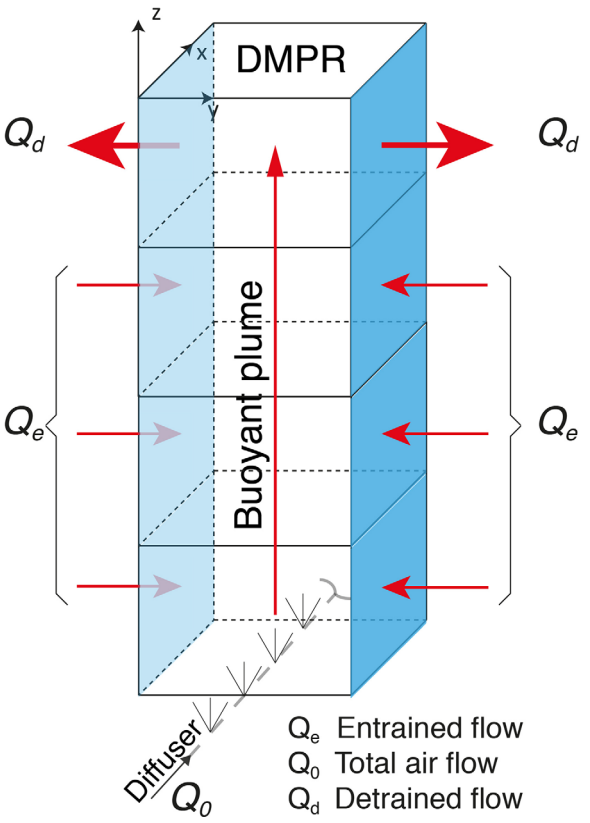

Figure 8. Schematic diagram of the bubble plume model within grid cells. The grid cells from the diffuser serve as sinks to relocate the plume water with entrainment successively from the lower to the upper grid cell. At the depth of the maximum plume rise, the grid cell serves as a source to discharge the plume.

The coupled water-jet model and the coupled bubble-plume model are further validated in the results and discussion section.

3.2. Coupled Bubble-Plume Model for EM

An existing linear bubble-plume model was employed to simulate mixing induced by the EM system, which releases air bubbles from a diffuser line within the metalimnion. The theory behind the bubble-plume model is well established [e.g., *Singleton and Little*, 2006; *Singleton et al*., 2007, 2010; *Wüest et al*., 1992], with a schematic representation of the model provided in Figure 8.

When a bubble-plume system is in operation, the buoyant plume entrains ambient water, traveling from the diffuser up to the depth of maximum plume rise (DMPR [*Singleton et al*., 2010]) where the momentum of the plume water reduces to zero and the water is detrained above its neutrally buoyant point. The bubble-plume model shown in Figure 8 is implemented as a series of sinks in Si3D using grid cells within the region between the diffuser depth and the model-estimated DMPR. The model successively relocates the water from the lower cell to the upper cell until the DMPR is reached, at which point the plume water is detrained into the horizontally adjacent grid cells. The model consists of a series of horizontally integrated equations based on conservation of mass, momentum, and heat. Additional flux equations are solved simultaneously to predict the flow rate of water, in-plume temperature, and oxygen transfer between the bubbles and the water [*Wüest et al*., 1992].

The linear bubble-plume model was validated by Singleton et al. [2007] in Spring Hollow Reservoir, VA, USA, where it was shown that plume temperature could be predicted to within 0.3°C, which is reasonable given the inherent complexity of the physical processes involved.

4. Results and Discussion

In this section, the influence of the SSS and EM systems on thermal stratification and DO is described based on the in situ experiments, which were carried out in 2015 (see Table 1). The coupled water-jet and bubble-plume models are also further validated against the field data.

4.1. Experimental Observations

The effects of the SSS and EM systems on water temperature and DO were investigated at FCR50, the deep end of the reservoir, as a function of time. The spatial extent of the effect was observed on the contours of the horizontal velocity across the EM diffuser line established by sampling along Transect #2, the location of which is shown in Figure 1a.

The time series of field temperature profiles (Figure 9a) at FCR50 showed that continuous operation of the SSS system mixed the hypolimnion, as also observed in the 2013 and 2014 tests [*Gerling et al*., 2014, 2016]. However, the hypolimnetic mixing induced by the SSS did not destratify the water body (as shown previously in Figures 6 and 7). Therefore, the SSS system only mixed the hypolimnion, as expected. In contrast, the operation of the EM system deepened the metalimnetic

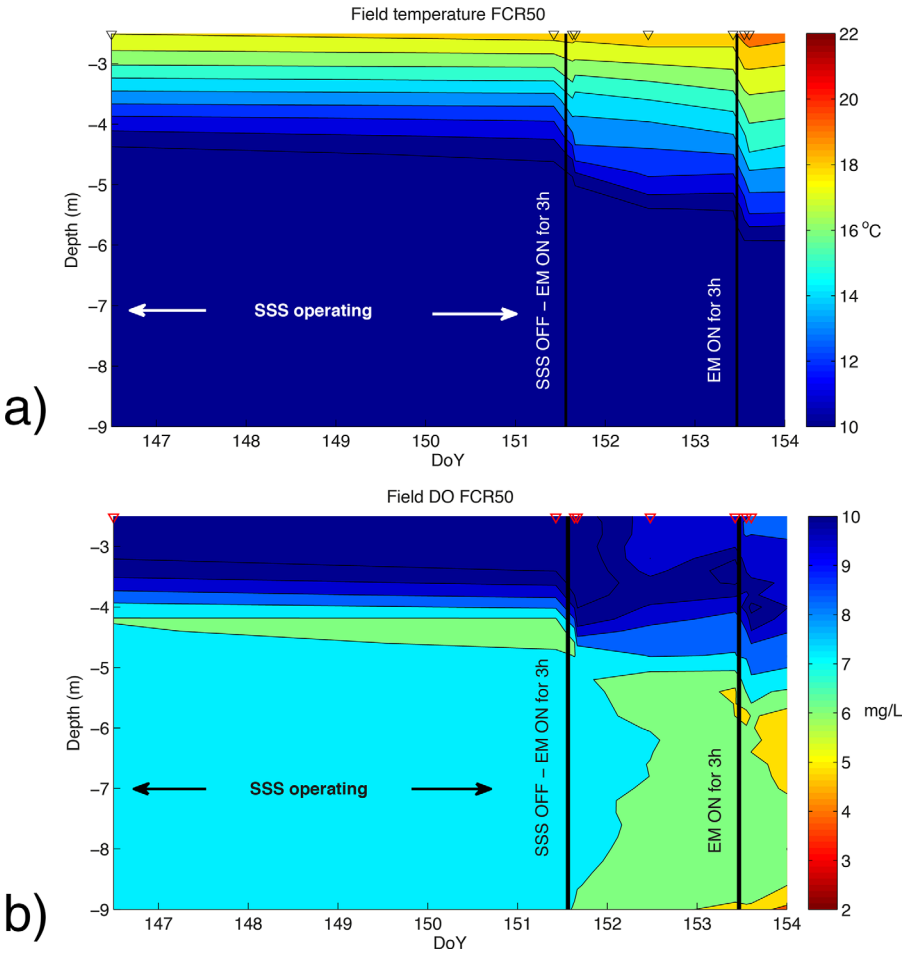

Figure 9. Temporal profile of field temperature and DO concentrations at FCR50 during the sequential operation of the SSS and EM systems (the oxygen contour level interval is 1 mg/L).

boundary, an effect that persisted long after the system was turned off on both occasions. Even though the EM system was only operated for 3 h each time, the mixing effect was significant. In addition to lowering the metalimnetic boundary, the surface mixed layer was expanded downward and the thermocline depth was deepened during the EM mixing period (refer to the time series of the thermocline depth in supporting information Figure S5), which is consistent with the goal of the EM system.

The field DO concentration in Figure 9b shows that the SSS system maintained the hypolimnetic DO concentration at expected levels (i.e., DO concentration above 7 mg/L), which means the SSS system successfully added DO to the hypolimnion, while the EM system mixed the DO in the metalimnion. From Day 147 to Day 151 when the SSS was in operation, the DO concentration fluctuated over the depth with the lowest concentration in the metalimnion. This phenomenon may have been caused by the weak vertical mixing induced by the SSS system. Once the SSS system was turned off, the DO concentration in the hypolimnion decreased rapidly, suggesting that the SSS may have stimulated additional oxygen demand [*Gantzer et al.*, 2009; *Gerling et al.*, 2014]. On the other hand, the EM homogenized the DO above the diffuser during the short operational period, indicating a much stronger vertical mixing effect compared to that induced by the SSS system.

To further understand the effect of mixing induced by the EM system, the thermal contours obtained from Transect #2 are shown in Figures 10a–10d. As shown in Table 1, the EM was operated intermittently. The following discussion focuses on the first 3-h operational period of the EM, because the change in thermal profiles during that time period was significant.

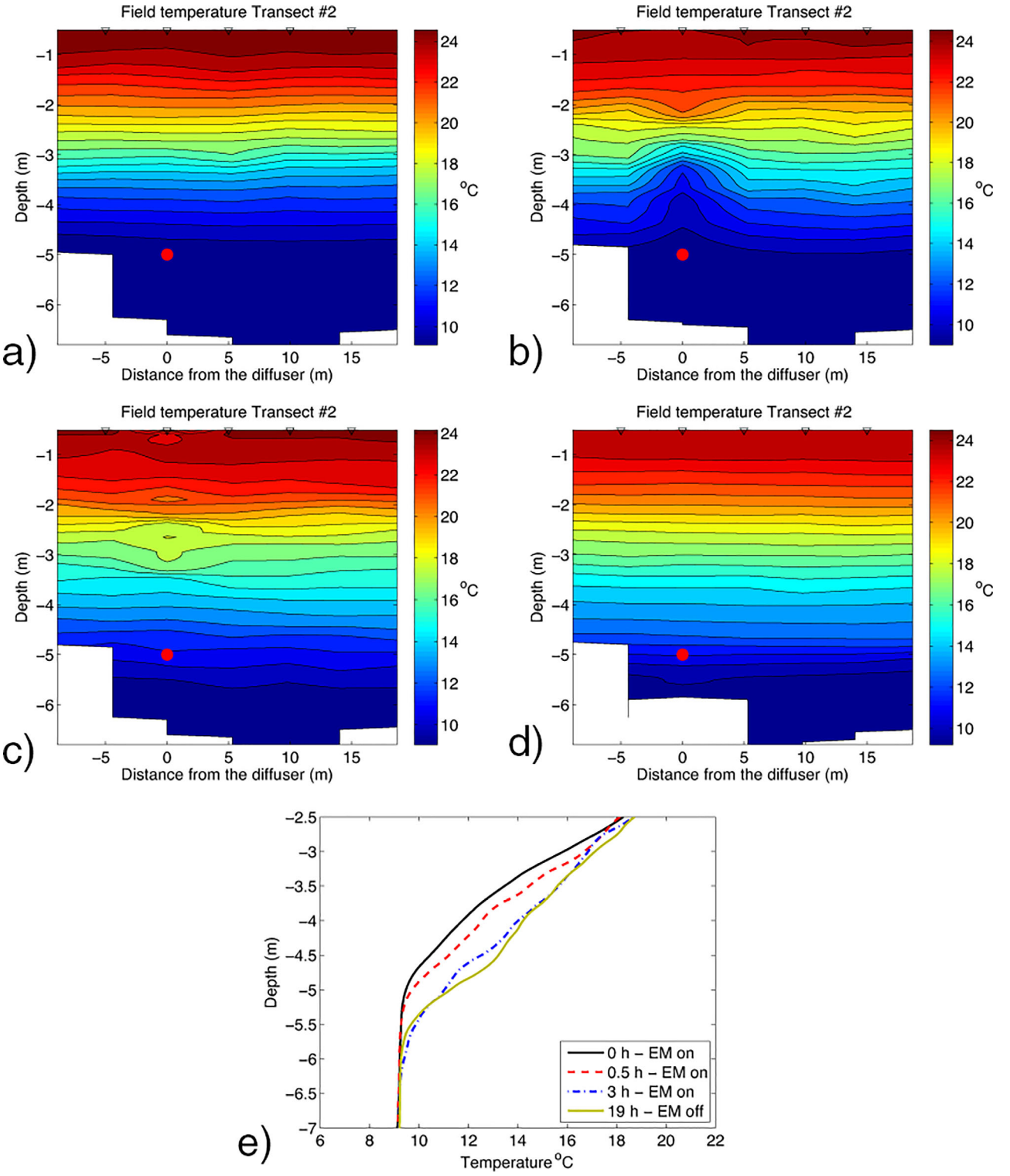

Figure 10. Field temperature profiles from Transect #2. (a) Immediately before the EM turned on; (b) 0.5 h after the EM turned on; (c) 3 h after the EM turned on; (d) approximately 1 day after the EM turned off. The red circle indicates where the diffuser line is located; and (e) time evolution of the depth profile of the field temperature at 10 m away from the diffuser line shown in (a)–(d) immediately after the EM was activated and 0.5, 3, and 19 h later. The EM was deactivated at 19 h.

In the first hour after the EM was activated, the bubble-plume entrained cold ambient water and then discharged it at the DMPR, causing recirculation and mixing between the DMPR and the depth of the diffuser. Little effect on the temperature was observed below the EM diffuser (Figure 10b). The cold water behaved

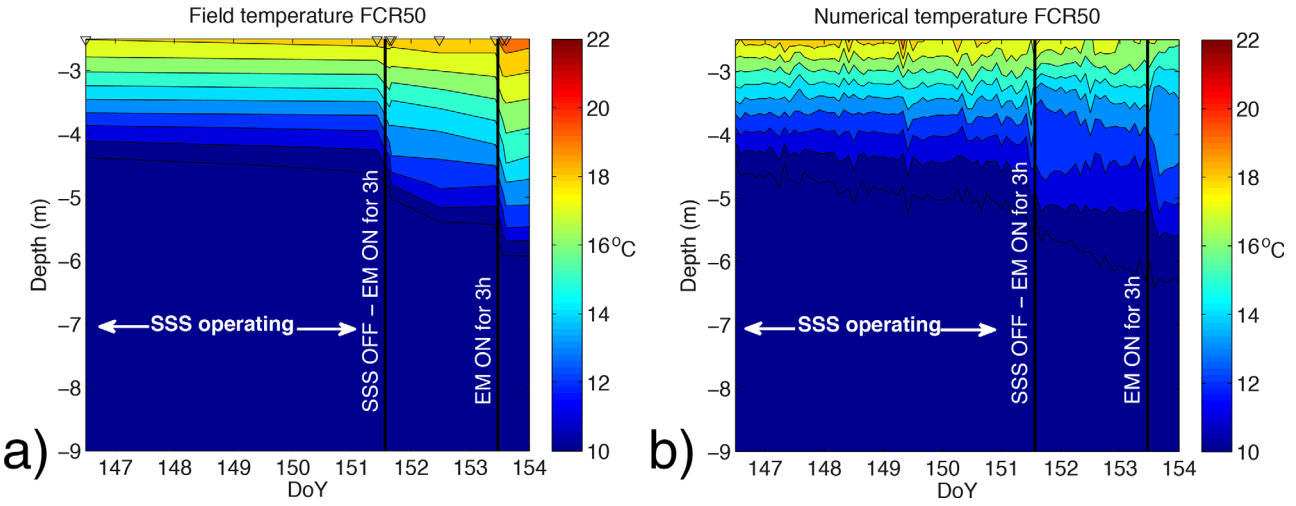

Figure 11. Time series of the field and numerical temperature contours at FCR50 during the sequential operation of the SSS and EM systems.

as a tracer in this early stage, indicating the plume development in the epilimnetic water. After 3 h of continuous operation, the water above the diffuser reached a quasi-steady state (Figure 10c), showing that the average metalimnetic temperature increased and that the metalimnetic boundary was significantly deepened because the EM diffuser was located near the depth of the initial metalimnetic boundary before the experiment. The depth change of the metalimnetic boundary is also shown in Figure 10e. After the EM was turned off, the mixing effect dissipated and the water column above 5 m depth became thermally stratified again. However, the level of the deepened metalimnetic boundary was maintained and the overall metalimnetic temperature slightly increased (Figure 10d). The increase of the water temperature after mixing is also shown in Figure 10e.

In summary, the SSS system successfully added DO to the hypolimnion without significantly changing the overall thermal structure in the reservoir, whereas the EM system mixed the surface mixed layer above the metalimnetic boundary, increasing the metalimnetic water temperature, and lowered the depth of the metalimnetic boundary.

4.2. Numerical Simulations

The numerical results obtained from the coupled Si3D model are now compared with the experimental observations. In this case, the coupled water-jet and bubble-plume models in Si3D described above were used to simulate mixing induced by the SSS and EM systems. The model settings followed the schedule given in Table 1.

The results obtained from the simulation are compared with the experimental data as discussed above. The comparison of the numerical and field temperature contours in Figure 11 shows that overall, the model predicted the development of the thermal structure and the level of mixing correctly. The temperature development was reasonably captured by the simulation. However, the numerical contours are noisier than the field contours. This is due to a much finer time resolution adopted in the numerical model compared to the field sampling.

The comparison of field and numerical temperature profiles at FCR50 in Figure 12 indicates that the numerical results agree well with the field data. In Figure 12a, both field and numerical results show that artificial mixing by the EM system increases the water temperature in the metalimnion, which tends to homogenize the temperature over the surface mixed layer, and thus reduce the temperature gradient in the metalimnion. Good consistency between the field and numerical results can also be seen in Figure 12b, where the depth of the metalimnetic boundary was lowered due to the mixing induced by the EM system. The comparison also confirms the findings from the field observations. In addition, the difference in the mean temperature of the water column between the field and numerical results is ~3.6% of the mean temperature in the field for the entire water column throughout the study period.

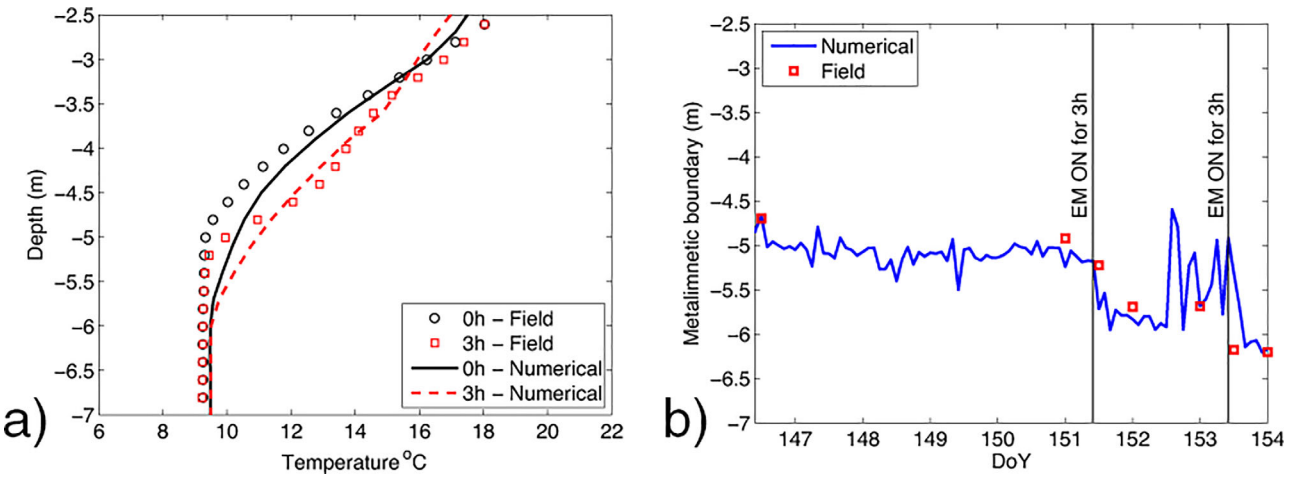

Figure 12. (a) Field temperature versus numerical temperature profiles at FCR50 before and after the EM on. (b) Time series of the depths of the metalimnetic boundary: field versus numerical data. The results were processed by the LakeAnalyzer program v3.3.3 [*Read et al.*, 2011].

5. Model Application

After validating against the in situ experimental results, we used Si3D to predict mixing under various operating conditions of the mixing devices, aiming to provide practical information for reservoir management. The extent to which the SSS and EM systems affect the thermal structure of the reservoir was investigated using Si3D with the two coupled models.

In this case, we used the meteorological data over the experimental period in 2015 and focused on the effects of the operational flow rates of the systems. Unlike the above discussion based on the field experiments, which shows the mixing effects under the specific experimental schedule, this case study provides additional insight into the mixing mechanisms, which may lead to the development of more effective operational procedures for the two systems. Two correlations between the thermal structure and flow rate of the devices are derived from the case study corresponding to the SSS and EM systems, respectively. For the SSS system (details are provided in supporting information Text S2), the relationship between the steepness (k) of the linear change of the depth of the metalimnetic boundary and the operational flow rate of the SSS system is characterized by the following simple exponential function:

$$k = -0.24e^{-0.004Q_{sss}} \tag{10}$$

where Q_{sss} represents the flow rate of the SSS system within the operational range in FCR. As the metalimnetic boundary is pushed downward, the value of the steepness (k) is negative. The minimum steepness is obtained when the flow rate of the SSS system is at a minimum (zero), which means the rate at which the metalimnetic boundary moves downward is highest. The result indicates that the hypolimnetic mixing induced by the SSS system reduces the rate at which the metalimnion expands toward the hypolimnion.

As for the EM system (refer to supporting information Text S3), the depth of the metalimnetic boundary that varies in the early stage of operation can be characterized by a double exponential function in terms of the duration of operation and the flow rate, i.e.,

$$h = \left(h_0 - 0.63{Q_{EM}}^{0.21}\right)e^{0.04t} + 0.63{Q_{EM}}^{0.21}e^{-1.72{Q_{EM}}^{0.24}t} \tag{11}$$

where h is the depth of the metalimnetic boundary measured from the water surface (negative) at time t; h_0 is the initial depth of the metalimnetic boundary; t is the duration of operation measured in days; and Q_{EM} represents the EM flow rate of air within the operational range in FCR. To explain this correlation further, there are two hypothesized processes involved with the EM operation. The positive term (second term) is related to the mixing by the EM system and the negative term (first term) characterizes the thermal diffusion. From the relationship, it is apparent that the EM term will be dominant at the beginning of the mixing process, elevating the horizontally homogenized thermal structure in the metalimnion by carrying the cold water from the level of the diffuser. But the effect of the EM term is weakened rapidly over time

during continuous operation because the metalimnetic boundary is pushed below the diffuser line, in which case the thermal diffusion term becomes increasingly important to the metalimnion development. The finding is consistent with the results shown in supporting information Figure S1 in Text S3.

These correlations represent an attempt to reveal mixing mechanisms induced by the SSS and EM systems, and can be used in planning future operation of the systems in FCR. For example, regular operation is required to maintain thermal structure during the stratified period. Due to the limited availability of field data, it is uncertain whether the fitted constants in the correlations can be generalized to other water bodies equipped with similar systems. However, the coupled hydrodynamic model Si3D should be able to predict the extent of artificial mixing in other water bodies with similar systems after model validation. Thus, a similar approach can be followed to develop correlations applicable to individual water bodies because the identified mixing mechanisms should be generally applicable.

6. Conclusions

Operation of both the SSS and EM systems is investigated experimentally and numerically. The field data are used to validate the numerical model, whereas the numerical results in conjunction with the field data reveal the effects of mixing on the thermal structure.

The present investigation reveals that the SSS system adds DO into the hypolimnetic water without destratifying the relatively shallow reservoir. The average hypolimnetic temperature is not substantially affected by the mixing caused by the SSS system. Further, the SSS system maintains the depth of the metalimnetic boundary by slowing down the development of stratification in the hypolimnion. The metalimnetic boundary is deepened more slowly during stratified periods with a higher SSS flow rate. In comparison, the EM system deepens the metalimnetic boundary significantly and mixes the surface mixed layer, as intended. An empirical correlation is developed to relate the depth of the metalimnetic boundary with the duration of operation and the EM air flow rate.

The investigation of the combined EM and SSS systems in sequential operation represents the first whole-reservoir experiment of its kind, and provides important insight into the potential effects of these management interventions. As SSS and EM systems are increasingly deployed, the present results can be used to inform the design and operation of SSS and EM systems in similar water bodies for enhanced water quality.

Acknowledgments
The data associated with this manuscript are available from the authors. We thank the Western Virginia Water Authority, especially R. Benninger, J. Booth, C. Brewer, P. Martin, J. Morris, and G. Robertson, for access to field sites and their support of this research. We thank J. P. Doubek, A. B. Gerling, K. D. Hamre, C. W. Harrell, R. P. McClure, and Z. W. Munger for their help in the field and lab. We acknowledge financial assistance from the William and Catherine McIlrath Scholarship and the Australian Postgraduate Award from The University of Sydney. This study was supported by the Fralin Life Sciences Institute and Global Change Center at Virginia Tech.

References

Bryant, L. D., P. A. Gantzer, and J. C. Little (2011), Increased sediment oxygen uptake caused by oxygenation-induced hypolimnetic mixing, *Water Res.*, *45*(12), 3692–3703.
Burris, V. L., D. F. McGinnis, and J. C. Little (2002), Predicting oxygen transfer and water flow rate in airlift aerators, *Water Res.*, *36*(18), 4605–4615.
Casulli, V., and R. T. Cheng (1990), Stability analysis of Eulerian-Lagrangian methods for the one-dimensional shallow-water equations, *Appl. Math. Modell.*, *14*(3), 122–131.
Casulli, V., and E. Cattani (1994), Stability, accuracy and efficiency of a semi-implicit method for three-dimensional shallow water flow, *Comput. Math. Appl.*, *27*(4), 99–112.
Chen, S., C. Lei, and J. C. Patterson (2014), Numerical modeling of a concurrent PIT/PIV experiment with TLC particles in a reservoir model subject to periodic thermal forcing, *Numer. Heat Transfer, Part A: Appl.*, *66*(1), 64–88.
Davison, W. (1993), Iron and manganese in lakes, *Earth Sci. Rev.*, *34*(2), 119–163.
Diaz, R. J. (2001), Overview of hypoxia around the world, *J. Environ. Qual.*, *30*(2), 275–281.
Fast, A. W., W. J. Overholtz, and R. A. Tubb (1975), Hypolimnetic oxygenation using liquid oxygen, *Water Resour. Res.*, *11*(2), 294–299.
Gantzer, P. A., L. D. Bryant, and J. C. Little (2009), Effect of hypolimnetic oxygenation on oxygen depletion rates in two water-supply reservoirs, *Water Res.*, *43*(6), 1700–1710.
Gerling, A. B., R. G. Browne, P. A. Gantzer, M. H. Mobley, J. C. Little, and C. C. Carey (2014), First report of the successful operation of a side stream supersaturation hypolimnetic oxygenation system in a eutrophic, shallow reservoir, *Water Res.*, *67*, 129–143.
Gerling, A. B., Z. W. Munger, J. P. Doubek, K. D. Hamre, P. A. Gantzer, J. C. Little, and C. C. Carey (2016), Whole-catchment manipulations of internal and external loading reveal the sensitivity of a century-old reservoir to hypoxia, *Ecosystems*, *19*(3), 555–571.
Hamilton, D. P., and S. G. Schladow (1997), Prediction of water quality in lakes and reservoirs. Part I — Model description, *Ecol. Modell.*, *96*(1–3), 91–110.
Imteaz, M. A., and T. Asaeda (2000), Artificial mixing of lake water by bubble plume and effects of bubbling operations on algal bloom, *Water Res.*, *34*(6), 1919–1929.
Imteaz, M. A., T. Asaeda, and D. A. Lockington (2003), Modelling the effects of inflow parameters on lake water quality, *Environ. Model. Assess.*, *8*(2), 63–70.
Imteaz, M. A., A. Shanableh, and T. Asaeda (2009), Modelling multi-species algal bloom in a lake and inter-algal competitions, *Water Sci. Technol.*, *60*(10), 2599–2611.

Kerimoglu, O., and K. Rinke (2013), Stratification dynamics in a shallow reservoir under different hydro-meteorological scenarios and operational strategies, *Water Resour. Res.*, *49*(11), 7518–7527, doi:10.1002/2013WR013520.
List, E. J. (1982), Mechanics of turbulent buoyant jets and plumes, in *Turbulent Buoyant Jets and Plumes*, edited by W. Rodi, pp. 1–68, Pergamon, Great Britain.
Lorenzen, M. W., and A. W. Fast (1977), *A Guide to Aeration/circulation Techniques for Lake Management*, Environmental Protection Agency, Office of Research and Development, Corvallis Environmental Research Laboratory, U. S.
Matthews, D. A., and S. W. Effler (2006), Assessment of long-term trends in the oxygen resources of a recovering Urban Lake, Onondaga Lake, New York, *Lake Reservoir Manage.*, *22*(1), 19–32.
McGinnis, D. F., and J. C. Little (1998), Bubble dynamics and oxygen transfer in a speece cone, *Water Sci. Technol.*, *37*(2), 285–292.
McGinnis, D. F., and J. C. Little (2002), Predicting diffused-bubble oxygen transfer rate using the discrete-bubble model, *Water Res.*, *36*(18), 4627–4635.
Monismith, S. G., J. Imberger, and M. L. Morison (1990), Convective motions in the sidearm of a small reservoir, *Limnol. Oceanogr.*, *35*(8), 1676–1702.
Mortimer, C. H. (1941), The exchange of dissolved substances between mud and water in lakes, *J. Ecol.*, *29*(2), 280–329.
Morton, B. R., G. Taylor, and J. S. Turner (1956), Turbulent gravitational convection from maintained and instantaneous sources, *Proc. R. Soc. London, Ser. A.*, *234*(1196), 1–23.
Nürnberg, G. K., B. D. LaZerte, and D. D. Olding (2003), An artificially induced *Planktothrix rubescens* surface bloom in a Small Kettle Lake in Southern Ontario compared to blooms world-wide, *Lake Reservoir Manage.*, *19*(4), 307–322.
Paillat, S., and E. Kaminski (2014), Second-order model of entrainment in planar turbulent jets at low Reynolds number, *Phys. Fluids*, *26*(4), 45110.
Read, J. S., D. P. Hamilton, I. D. Jones, K. Muraoka, L. A. Winslow, R. Kroiss, C. H. Wu, and E. Gaiser (2011), Derivation of lake mixing and stratification indices from high-resolution lake buoy data, *Environ. Modell. Software*, *26*(11), 1325–1336.
Rueda, F., V. Singleton, M. Stewart, J. Little, and G. Lawrence (2010), Modeling the fate of oxygen artificially injected in the hypolimnion of a lake with multiple basins: Amisk Lake revisited, in *Paper presented at Environmental Hydraulics - Proceedings of the 6th International Symposium on Environmental Hydraulics*, Netherlands.
Rueda, F. J., E. Sanmiguel-Rojas, and B. R. Hodges (2007), Baroclinic stability for a family of two-level, semi-implicit numerical methods for the 3D shallow water equations, *Int. J. Numer. Methods Fluids*, *54*(3), 237–268.
Singleton, V. L., and J. C. Little (2006), Designing hypolimnetic aeration and oxygenation systems - A review, *Environ. Sci. Technol.*, *40*(24), 7512–7520.
Singleton, V. L., P. Gantzer, and J. C. Little (2007), Linear bubble plume model for hypolimnetic oxygenation: Full-scale validation and sensitivity analysis, *Water Resour. Res.*, *43*, W02405, doi:10.1029/2005WR004836.
Singleton, V. L., F. J. Rueda, and J. C. Little (2010), A coupled bubble plume-reservoir model for hypolimnetic oxygenation, *Water Resour. Res.*, *46*, W12538, doi:10.1029/2009WR009012.
Smith, P. E. (2006), A semi-implicit, three-dimensional model for estuarine circulation, *U.S. Geological Survey Open-File Report 2006–1004*, U. S.
Toffolon, M., and M. Serafini (2013), Effects of artificial hypolimnetic oxygenation in a shallow lake. Part 2: Numerical modelling, *J. Environ. Manage.*, *114*, 530–539.
Toffolon, M., M. Ragazzi, M. Righetti, C. R. Teodoru, M. Tubino, C. Defrancesco, and S. Pozzi (2013), Effects of artificial hypolimnetic oxygenation in a shallow lake. Part 1: Phenomenological description and management, *J. Environ. Manage.*, *114*, 520–529.
Valiela, I., J. McClelland, J. Hauxwell, P. J. Behr, D. Hersh, and K. Foreman (1997), Macroalgal blooms in shallow estuaries: Controls and ecophysiological and ecosystem consequences, *Limnol. Oceanogr.*, *42*(5 II), 1105–1118.
Vilhena, L. C., I. Hillmer, and J. Imberger (2010), The role of climate change in the occurrence of algal blooms: Lake Burragorang, Australia, *Limnol. Oceanogr.*, *55*(3), 1188–1200.
Visser, P., B. Ibelings, M. Bormans, and J. Huisman (2016), Artificial mixing to control cyanobacterial blooms: A review, *Aquat Ecol.*, *50*(3), 423–441.
Walsby, A. E. (2005), Stratification by cyanobacteria in lakes: A dynamic buoyancy model indicates size limitations met by Planktothrix rubescens filaments, *New Phytol.*, *168*(2), 365–376.
Walsby, A. E., F. Schanz, and M. Schmid (2006), The Burgundy-blood phenomenon: A model of buoyancy change explains autumnal waterblooms by Planktothrix rubescens in Lake Zürich, *New Phytol.*, *169*(1), 109–122.
Wang, H., and A. Wing-Keung Law (2002), Second-order integral model for a round turbulent buoyant jet, *J. Fluid Mech.*, *459*, 397–428.
Wüest, A., N. H. Brooks, and D. M. Imboden (1992), Bubble plume modeling for lake restoration, *Water Resour. Res.*, *28*(12), 3235–3250.
Xu, G., and R. Antonia (2002), Effect of different initial conditions on a turbulent round free jet, *Exp. Fluids*, *33*(5), 677–683.